

# Coreactant Strategy for the Photoredox Catalytic Generation of Trifluoromethyl Radicals under Low-Energy Photoirradiation

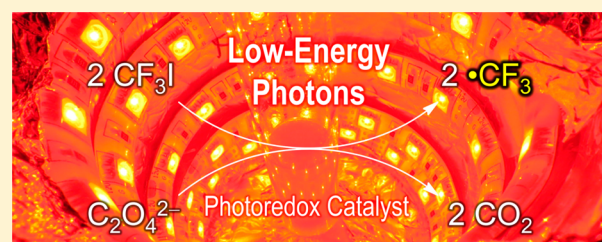
Sinheui Kim,<sup>†</sup> Gyurim Park,<sup>‡</sup> Eun Jin Cho,<sup>\*,§</sup> and Youngmin You<sup>\*,†</sup>

<sup>†</sup>Division of Chemical Engineering and Materials Science and <sup>‡</sup>Department of Food Science, Ewha Womans University, Seoul 03760, Republic of Korea

<sup>§</sup>Department of Chemistry, Chung-Ang University, Seoul 06974, Republic of Korea

**S** Supporting Information

**ABSTRACT:** Photoredox catalysis has emerged as a valuable alternative to dark-state catalysis. For the full potential of photoredox catalysis to be utilized, it is imperative to make use of low-energy photons in photoinduced radical processes. We have demonstrated that the use of oxalate as a coreactant provides a useful principle for the photocatalytic production of trifluoromethyl radicals ( $\bullet\text{CF}_3$ ) from  $\text{CF}_3\text{I}$  upon green or red LED photoirradiation of narrow-bandgap photocatalysts. The photocatalytic cycle involves a radical anion of carbon dioxide ( $\text{CO}_2^{\bullet-}$ ) as a reductant for  $\text{CF}_3\text{I}$ , which is generated through photoinduced oxidative decarboxylation of oxalate. Electrochemical characterizations and steady-state and transient photophysical investigations were performed to reveal that there are two photoinduced electron-transfer pathways for oxalate-mediated  $\bullet\text{CF}_3$  generation.



## I. INTRODUCTION

Photoredox catalysis has recently been recognized as a powerful tool for radical-mediated organic transformations.<sup>1–20</sup> One particular advantage of photoredox catalysis is the generation of thermodynamically challenging radical intermediates, such as trifluoromethyl radicals ( $\bullet\text{CF}_3$ ), under mild reaction conditions. Transition metal complexes, such as those containing Ir(III),<sup>21–25</sup> Ru(II),<sup>21,22,24,26–38</sup> and Pt(II),<sup>39</sup> are employed to catalyze the reductive cleavage of electrophilic  $\bullet\text{CF}_3$  precursors upon visible light irradiation. It is envisioned that benefits of the photoredox catalysis can be maximized if the processes are steered by a solar photon. However, it is noted that the majority of the reported photoredox catalytic trifluoromethylation reactions have been carried out under blue LED photoirradiation. The necessity of such high-energy photon sources stems from the thermodynamic requirement that the ground-state reduction potentials or excited-state oxidation potentials of the catalysts should be as negative as possible to enable exergonic electron transfer to the  $\bullet\text{CF}_3$  precursors. This thermodynamic condition can be met for wide-bandgap catalysts, but such catalysts cannot be used in redox catalysis under low-energy photoirradiation. The activation of less-reactive radical precursors by low-energy photons remains a significant challenge, and successful demonstrations have only sporadically been reported.<sup>40–44</sup>

We propose a coreactant strategy that addresses this difficulty (see Scheme 1). The one-electron oxidation of oxalate ( $\text{C}_2\text{O}_4^{2-}$ ;  $E_{\text{ox}} = 0.21$  V vs SCE,  $\text{CH}_3\text{CN}$ ) facilitates the fast homolytic cleavage of the C–C bond in oxalate, furnishing  $\text{CO}_2$  and the radical anion of  $\text{CO}_2$  ( $\text{CO}_2^{\bullet-}$ ) (i.e.,  $\text{C}_2\text{O}_4^{2-} \rightarrow \text{C}_2\text{O}_4^{\bullet-} + e^-$ , followed by  $\text{C}_2\text{O}_4^{\bullet-} \rightarrow \text{CO}_2 + \text{CO}_2^{\bullet-}$ ).<sup>26,45,46</sup> The latter

product ( $\text{CO}_2^{\bullet-}$ ) possesses a very negative oxidation potential,  $-2.20$  V vs SCE,<sup>47–49</sup> thus, it would be capable of the one-electron reduction of common electrophilic  $\bullet\text{CF}_3$  sources, including  $\text{CF}_3\text{I}$  ( $E_{\text{red}} = -0.91$  V vs SCE,  $\text{CH}_3\text{CN}$ ).<sup>50</sup> Actually, one electron transfer from  $\text{CO}_2^{\bullet-}$  to  $\text{CF}_3\text{I}$  is predicted to be highly exergonic with a driving force for electron transfer as large as 1.29 eV, which cannot be achieved with conventional visible-light photoredox catalysts. In addition to such high exothermicity, the redox processes mediated by oxalate have the significant advantage that any photoredox catalyst with excited-state reduction potentials more positive than 0.21 V vs SCE can catalyze  $\bullet\text{CF}_3$  generation. Decoupling the two key processes of the photocatalysis (i.e., photon absorption by a photocatalyst and electron transfer from  $\text{CO}_2^{\bullet-}$  to a  $\bullet\text{CF}_3$  precursor) means that a wide range of photocatalysts can be used and enables  $\bullet\text{CF}_3$  generation by using low-energy photons. Furthermore, the strategy effectively suppresses hazardous charge recombination between gaseous  $\text{CO}_2$  and the one electron-reduced species of a  $\bullet\text{CF}_3$  precursor.

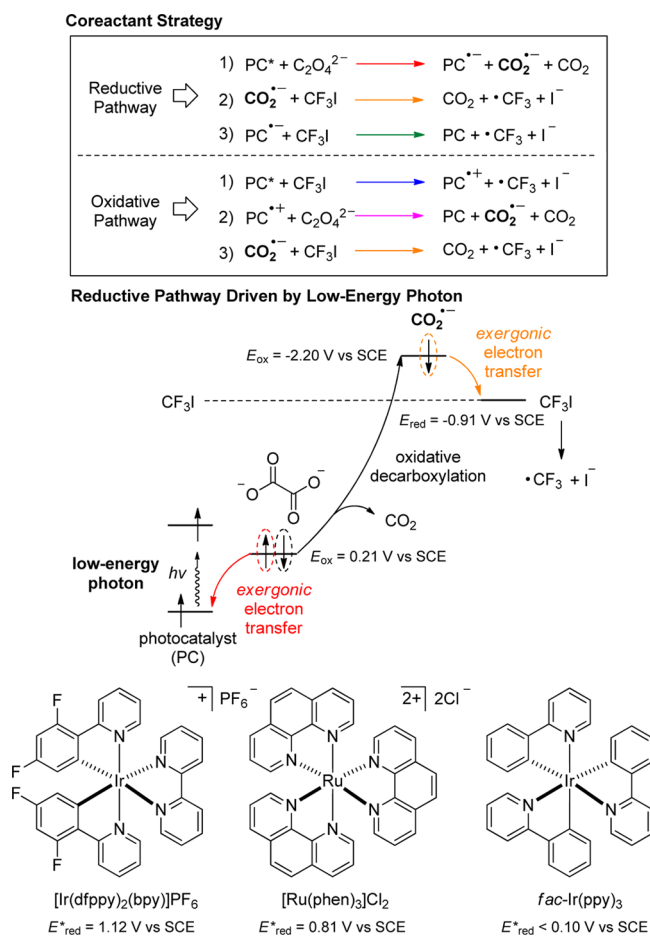
The high reducing power of  $\text{CO}_2^{\bullet-}$  has been thoroughly investigated and demonstrated to be very useful.<sup>51–54</sup> For instance, Bard and co-workers established the unique reduction ability of oxalate for electrochemoluminescence applications.<sup>46,47,55,56</sup> Kinetic aspects of electron transfer behaviors of oxalate have also previously been investigated.<sup>57,58</sup> In particular, Fukuzumi and co-workers employed oxalate as a

**Special Issue:** Photocatalysis

**Received:** April 28, 2016

**Published:** June 3, 2016

### Scheme 1. Chemical Equations for the Coreactant Strategy and a Schematic Representation of the Low-Energy Photoredox Catalytic Generation of Trifluoromethyl Radicals in the Presence of an Oxalate Coreactant with the Molecular Structures for the Photoredox Catalysts (PCs) Employed in This Study



two-electron source for the photocatalytic production of  $H_2$ <sup>59</sup> and  $H_2O_2$ .<sup>60</sup> Building on these studies, we propose a strategy for low-energy photoredox catalytic trifluoromethylation that employs oxalate as a coreactant. We primarily focus on the mechanism of photoinduced electron transfer between the photocatalysts and the oxalate coreactant. Finally, we demonstrate that the coreactant strategy enables the photoredox catalytic generation of  $\bullet CF_3$  under photoirradiation with green and red LEDs. Note that the production of  $\bullet CF_3$  with low-energy photoirradiation, such as that of red LEDs, is unprecedented.

## II. RESULTS AND DISCUSSION

We employed tetrabutylammonium oxalate (TBAOX) as the oxalate source<sup>47,55,56</sup> because it exhibits high solubility in acetonitrile. Three different classes of photoredox catalysts, including a dicationic Ru(II) diimine complex,  $[Ru(phen)_3]Cl_2$  (phen = 1,10-phenanthroline), a cationic biscyclometalated Ir(III) complex,  $[Ir(dfppy)_2(bpy)]PF_6$  (dfppy = 2-(2,4-difluorophenyl)pyridinato; bpy = 2,2'-bipyridine), and a charge-neutral tricyclometalated Ir(III) complex,  $fac-Ir(ppy)_3$  (ppy = 2-phenylpyridinato) were selected because they have varied electrochemical potentials with almost identical metal-to-

ligand charge transfer (MLCT) transition energies ( $\lambda_{abs}(MLCT)$ ):  $[Ru(phen)_3]Cl_2$ , 447 nm;  $[Ir(dfppy)_2(bpy)]PF_6$ , 442 nm;  $fac-Ir(ppy)_3$ , 450 nm; see Figure S1 in the Supporting Information (SI)). The catalysts exhibited the ground- and excited-state redox potentials in an increasing order of  $fac-Ir(ppy)_3 < [Ru(phen)_3]Cl_2 < [Ir(dfppy)_2(bpy)]PF_6$  (vide infra). We envisioned this selection of the photoredox catalysts would provide an ideal opportunity to systematically investigate a series of electron-transfer reactions with minimal variation in photon absorption.

The ground-state reduction ( $E_{red}$ ) and oxidation ( $E_{ox}$ ) potentials were determined by employing cyclic voltammetry in acetonitrile solutions and verified with differential pulse voltammetry (Figure S2). The excited-state reduction ( $E_{red}^*$ ) and oxidation ( $E_{ox}^*$ ) potentials were calculated using the relationships  $E_{red}^* = E_{red} + \Delta E_T$  and  $E_{ox}^* = E_{ox} - \Delta E_T$ , where  $\Delta E_T$  is the peak wavelength of the phosphorescence spectrum (Figure S3). Figure 1 depicts a schematic representation of the

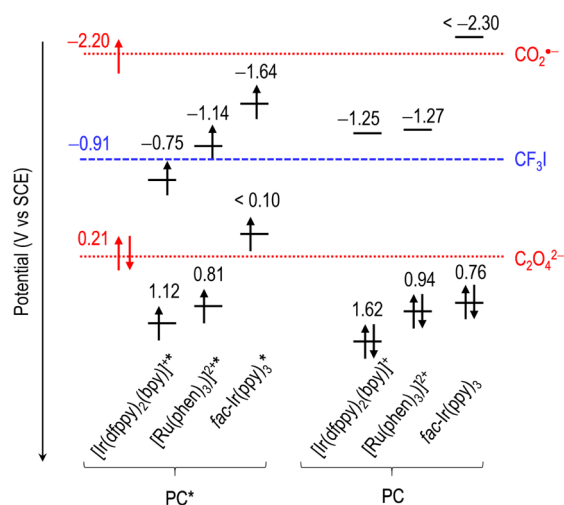


**Figure 1.** Comparison of the electrochemical potentials of the photoexcited states ( $PC^*$ ) and ground states ( $PC$ ) of the photocatalysts (black), the reduction potential of  $CF_3I$  (blue), and the oxidation potentials of  $C_2O_4^{2-}$  (red) and  $CO_2^{\bullet-}$  (red).

$E_{ox}$ ,  $E_{red}$ ,  $E_{ox}^*$ , and  $E_{red}^*$  values of the three photocatalysts along with the  $E_{red}$  value of  $CF_3I$  and the  $E_{ox}$  values of  $C_2O_4^{2-}$  and  $CO_2^{\bullet-}$ , which suggests that  $[Ir(dfppy)_2(bpy)]PF_6$  and  $[Ru(phen)_3]Cl_2$  will be capable of the oxidation of oxalate in their photoexcited states. The driving forces for the photoinduced one-electron oxidation of oxalate ( $-\Delta G_{PC^*(red)}$ ) were estimated using the Rehm–Weller equation  $-\Delta G_{PC^*(red)} = e \cdot [E_{ox}(C_2O_4^{2-}) - E_{red}^*(PC)]$  to be 0.91 and 0.60 eV for  $[Ir(dfppy)_2(bpy)]PF_6$  and  $[Ru(phen)_3]Cl_2$ , respectively, where  $e$ ,  $E_{ox}(C_2O_4^{2-})$ , and  $E_{red}^*(PC)$  are the elementary charge of an electron, the  $E_{ox}$  value of oxalate, and the  $E_{red}^*$  value of the photocatalyst ( $PC$ ), respectively. A negative  $-\Delta G_{PC^*(red)}$  value is predicted for  $fac-Ir(ppy)_3$ , which implies that reductive quenching by TBAOX cannot occur. The one-electron-oxidized oxalate ( $C_2O_4^{\bullet-}$ ) undergoes C–C bond cleavage to yield  $CO_2$  and  $CO_2^{\bullet-}$ . Subsequent electron transfer from  $CO_2^{\bullet-}$  to  $CF_3I$  with a driving force of 1.29 eV yields  $\bullet CF_3$ . Finally, the photocatalytic cycle is completed through the neutralization of the one-electron-reduced photocatalysts by electron transfer to  $CF_3I$  with driving forces of 0.34 and 0.36 eV for  $[Ir(dfppy)_2(bpy)]PF_6$  and  $[Ru(phen)_3]Cl_2$ , respectively. The

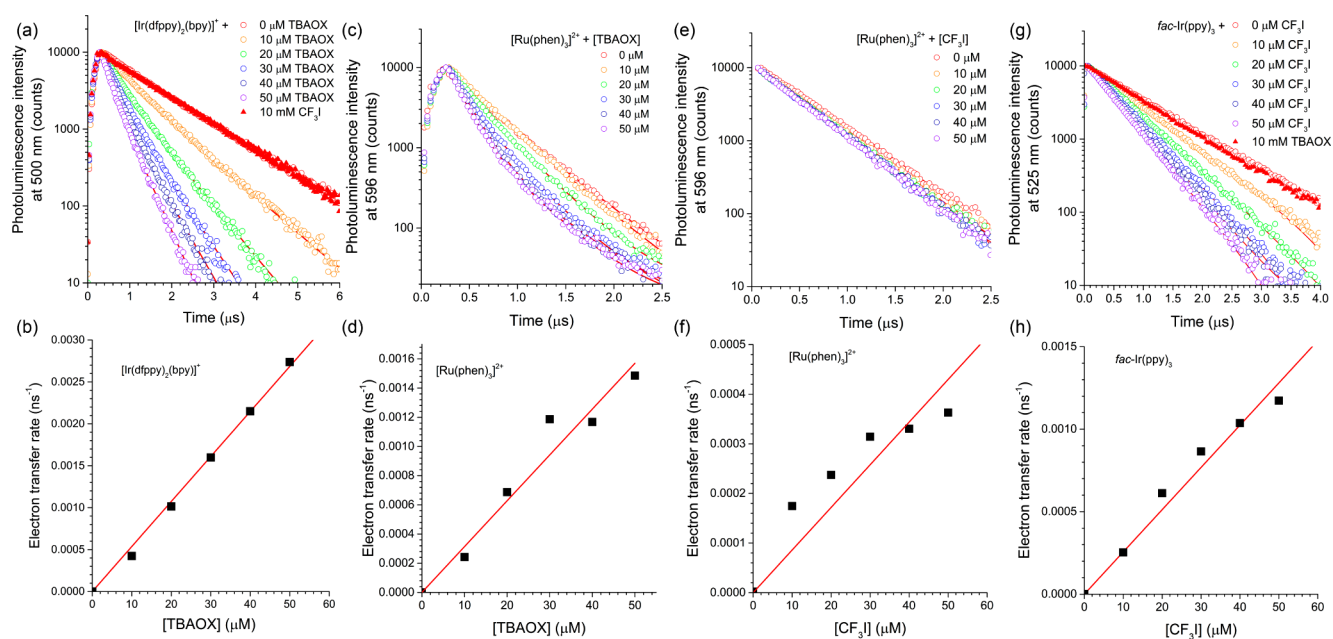
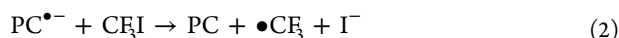


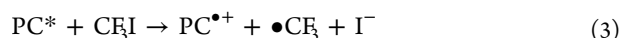
**Figure 2.** Monitoring the photoinduced electron transfer processes of the catalysts. Photoluminescence decay traces of 50  $\mu\text{M}$   $[\text{Ir}(\text{dfppy})_2(\text{bpy})]^+$  (a;  $\lambda_{\text{obs}} = 500 \text{ nm}$ ), 50  $\mu\text{M}$   $[\text{Ru}(\text{phen})_3]^{2+}$  (c and e;  $\lambda_{\text{obs}} = 596 \text{ nm}$ ), and 50  $\mu\text{M}$   $\text{fac-Ir}(\text{ppy})_3$  (g;  $\lambda_{\text{obs}} = 525 \text{ nm}$ ) upon nanosecond pulsed laser excitation at 377 nm (temporal resolution = 32 ns) with increases in the concentration (0–50  $\mu\text{M}$ ) of TBAOX (a and c) or  $\text{CF}_3\text{I}$  (e and g). The red curves are nonlinear least-squares fits to monoexponential (a, e, and g) and biexponential (c) decay models. Corresponding pseudo linear plots of the electron transfer rates of  $[\text{Ir}(\text{dfppy})_2(\text{bpy})]^+$  (b),  $[\text{Ru}(\text{phen})_3]^{2+}$  (d and f), and  $\text{fac-Ir}(\text{ppy})_3$  (h) as functions of the added concentrations of TBAOX (b and d) or  $\text{CF}_3\text{I}$  (f and h). Photoluminescence decay traces for  $[\text{Ir}(\text{dfppy})_2(\text{bpy})]^+$  in the presence of 10 mM  $\text{CF}_3\text{I}$  (a) and for  $\text{fac-Ir}(\text{ppy})_3$  in the presence of 10 mM TBAOX (g) are also shown (red filled triangles).

driving force for each electron transfer ( $-\Delta G_{\text{PC}^{\bullet-}}$ ) can be calculated with the relationship  $-\Delta G_{\text{PC}^{\bullet-}} = e \cdot [E_{\text{red}}(\text{PC}) - E_{\text{red}}(\text{CF}_3\text{I})]$ , where  $E_{\text{red}}(\text{PC})$  and  $E_{\text{red}}(\text{CF}_3\text{I})$  are the  $E_{\text{red}}$  values of the photocatalyst and  $\text{CF}_3\text{I}$ , respectively. This analysis reveals that there are two processes that produce  $\bullet\text{CF}_3$  (eqs 1 and 2)



The latter process (eq 2) is identical to the reductive quenching pathway of conventional photoredox catalysis.<sup>22,23,28,32–34,61</sup> Note that the driving force for  $\bullet\text{CF}_3$  generation of the former process (eq 1;  $-\Delta G = 1.29 \text{ eV}$ ) is larger than those of the latter processes (eq 2) for  $[\text{Ru}(\text{phen})_3]\text{Cl}_2$  ( $-\Delta G_{\text{PC}^{\bullet-}} = 0.36 \text{ eV}$ ) and  $[\text{Ir}(\text{dfppy})_2(\text{bpy})]\text{PF}_6$  ( $-\Delta G_{\text{PC}^{\bullet-}} = 0.34 \text{ eV}$ ).

An alternative pathway is available for the photoredox catalytic generation of  $\bullet\text{CF}_3$ . Of the three catalysts,  $[\text{Ru}(\text{phen})_3]\text{Cl}_2$  and  $\text{fac-Ir}(\text{ppy})_3$  are capable of oxidative electron transfer to  $\text{CF}_3\text{I}$  under photoirradiation with driving forces ( $-\Delta G_{\text{PC}^*(\text{ox})}$ ) of 0.23 and 0.73 eV, respectively. Such driving force is estimated by the relationship  $-\Delta G_{\text{PC}^*(\text{ox})} = e \cdot [E_{\text{ox}}^*(\text{PC}) - E_{\text{red}}(\text{CF}_3\text{I})]$ , where  $E_{\text{ox}}^*(\text{PC})$  is the  $E_{\text{ox}}^*$  value of the photocatalyst. This oxidative quenching is not possible for  $[\text{Ir}(\text{dfppy})_2(\text{bpy})]\text{PF}_6$  due to the negative driving force ( $-0.16 \text{ eV}$ ). After oxidative quenching by  $\text{CF}_3\text{I}$ , the resulting one-electron-oxidized photocatalysts are neutralized by oxalate with driving forces for electron transfer of 0.73 and 0.55 eV for  $[\text{Ru}(\text{phen})_3]\text{Cl}_2$  and  $\text{fac-Ir}(\text{ppy})_3$ , respectively. This process also generates  $\text{CO}_2^{\bullet-}$ , which can reductively cleave  $\text{CF}_3\text{I}$  into  $\bullet\text{CF}_3$  and iodide. In analogy with the reductive pathway, there are two processes for  $\bullet\text{CF}_3$  formation in the presence of  $[\text{Ru}(\text{phen})_3]\text{Cl}_2$  and  $\text{fac-Ir}(\text{ppy})_3$  (eqs 1 and 3)



The above thermodynamic considerations predict that the overall reaction can be understood as two-electron transfer from oxalate to two molecules of  $\text{CF}_3\text{I}$ :  $\text{C}_2\text{O}_4^{2-} + 2 \text{CF}_3\text{I} \rightarrow 2 \text{CO}_2 + 2 \bullet\text{CF}_3 + 2 \text{I}^-$ . This reaction can be initiated upon photoirradiation through either a reductive quenching pathway ( $[\text{Ir}(\text{dfppy})_2(\text{bpy})]\text{PF}_6$  and  $[\text{Ru}(\text{phen})_3]\text{Cl}_2$ ) or an oxidative quenching pathway ( $[\text{Ru}(\text{phen})_3]\text{Cl}_2$  and  $\text{fac-Ir}(\text{ppy})_3$ ). To directly probe these quenching pathways, photoluminescence decay traces for the photocatalysts (50  $\mu\text{M}$  in Ar-saturated acetonitrile solutions) were monitored by employing time-correlated single-photon-counting techniques after nanosecond-pulsed laser excitation at 377 nm. The excited states of the photocatalysts were long-lived with observed lifetimes ( $\tau_{\text{obs}}$ ) of 1.2  $\mu\text{s}$  ( $[\text{Ir}(\text{dfppy})_2(\text{bpy})]\text{PF}_6$ ), 0.44  $\mu\text{s}$  ( $[\text{Ru}(\text{phen})_3]\text{Cl}_2$ ), and 1.5  $\mu\text{s}$  ( $\text{fac-Ir}(\text{ppy})_3$ ). Increasing the concentration of TBAOX in the  $[\text{Ir}(\text{dfppy})_2(\text{bpy})]\text{PF}_6$  and  $[\text{Ru}(\text{phen})_3]\text{Cl}_2$  solutions leads to decreases in  $\tau_{\text{obs}}$  (Figures 2a and c), as is consistent with our thermodynamic predictions. Electron-transfer rates were calculated using the equation electron transfer rate =  $1/\tau_{\text{obs}} - 1/\tau_{\text{obs}(0)}$ , where  $\tau_{\text{obs}}$  and  $\tau_{\text{obs}(0)}$  are the photoluminescence lifetimes in the presence and absence of TBAOX, respectively. Pseudo first-order plots of the electron-transfer rates as functions of the concentration of TBAOX yield the following rate constants for the bimolecular reductive quenching of the catalysts:  $5.5 \times 10^{10}$  and  $2.8 \times 10^{10} \text{ M}^{-1} \text{ s}^{-1}$  for  $[\text{Ir}(\text{dfppy})_2(\text{bpy})]\text{PF}_6$  and  $[\text{Ru}(\text{phen})_3]\text{Cl}_2$ , respectively (Figure 2b and d). These rate constants approach the diffusion rate constant in acetonitrile at 298 K ( $\sim 10^{10} \text{ M}^{-1} \text{ s}^{-1}$ ), which indicates the occurrence of ultrafast electron transfer. As expected, the photoluminescence decay profile for  $\text{fac-Ir}(\text{ppy})_3$  is not affected by the presence of TBAOX (red filled triangles in Figure 2g).



In sharp contrast, the photoexcited state of *fac*-Ir(ppy)<sub>3</sub> is oxidatively quenched by CF<sub>3</sub>I (Figure 2g and h). The rate constant for oxidative electron transfer was determined to be as large as  $2.6 \times 10^{10} \text{ M}^{-1} \text{ s}^{-1}$ . Such oxidative quenching by CF<sub>3</sub>I is also evident for [Ru(phen)<sub>3</sub>]Cl<sub>2</sub> at a rate constant of  $8.6 \times 10^9 \text{ M}^{-1} \text{ s}^{-1}$  (Figures 2e and f), which is 1 order of magnitude smaller than the value for reductive quenching by TBAOX. This result indicates the propensity of the reductive quenching pathway in [Ru(phen)<sub>3</sub>]Cl<sub>2</sub>, as suggested by the driving forces (i.e., 0.60 eV (reductive quenching) vs 0.23 eV (oxidative quenching)). As expected, [Ir(dfppy)<sub>2</sub>(bpy)]PF<sub>6</sub> does not undergo oxidative quenching by CF<sub>3</sub>I (Figure 2a). Steady-state photoluminescence quenching experiments also revealed the exclusive occurrence of reductive quenching of [Ir(dfppy)<sub>2</sub>(bpy)]PF<sub>6</sub> by oxalate (Figure S4). Thus, we conclude that the use of [Ir(dfppy)<sub>2</sub>(bpy)]PF<sub>6</sub> selects the reductive quenching pathway in the presence of TBAOX, whereas *fac*-Ir(ppy)<sub>3</sub> follows the oxidative quenching pathway in the presence of CF<sub>3</sub>I. In the case of [Ru(phen)<sub>3</sub>]<sub>2</sub>, both quenching routes are available.

The rate constants for the initial electron-transfer reactions ( $k_{\text{eT}}$ ) can be correlated with their respective driving force values in a Marcus-type plot.<sup>62–64</sup> As displayed in Figure 3, the

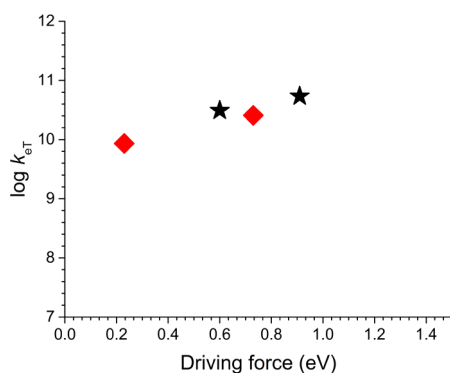


**Figure 3.** Correlation of the  $\log k_{\text{eT}}$  values and driving forces for reductive electron transfer (black stars) and oxidative electron transfer (red diamonds).

electron transfer is located on the plateau of the Marcus curve of electron transfer. This result indicates that the initial electron transfer is not a rate-determining step in the overall  $\bullet\text{CF}_3$  generation processes. In addition, the reductive electron transfer from oxalate to the photoexcited catalysts is more favored.

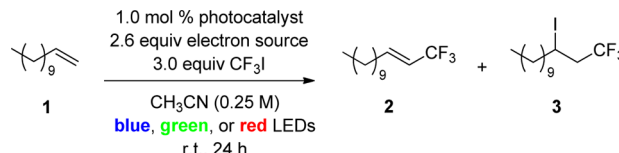
The synthetic utility of the oxalate coreactant strategy was tested for Ar-saturated acetonitrile solutions containing 0.25 M 1-dodecene, 0.75 M CF<sub>3</sub>I, 0.65 M TBAOX, and 1 mol % photocatalyst. 1-Dodecene (**1**) was chosen as the substrate for  $\bullet\text{CF}_3$  because our previous studies indicated that the terminal alkene can readily trap  $\bullet\text{CF}_3$ .<sup>39</sup> The reaction mixtures were photoirradiated with blue LEDs (4 W) at room temperature for 24 h; then, GC–MS analyses were performed by using dodecane as an internal standard. Note that the reaction conditions were not optimized and that further synthetic elaborations are required to obtain the best results. As summarized in Table 1, the photoirradiations yielded a mixture of a trifluoromethylated alkene (**2**) and an iodotrifluoromethylated product (**3**). Hydrotrifluoromethylation products (**4** in Scheme 2) were also generated in 2–10%. This outcome resulted from a common intermediate. As shown in Scheme 2,

the addition of  $\bullet\text{CF}_3$  to **1** generates **1a**, which can be oxidized into carbocation intermediate **1b**. Deprotonation of **1b** by oxalate or solvent molecules yields alkene product **2**, whereas nucleophilic addition of iodide furnishes iodotrifluoromethylation product **3**. Alternatively, **1a** can undergo a radical propagation reaction with CF<sub>3</sub>I to yield **3**, as we proposed in our previous studies.<sup>39</sup> Finally, hydrogen atom abstraction from solvents produces hydrotrifluoromethylation product **4**.

Control experiments performed in the dark (entry 2) or in the absence of oxalate (entry 3) demonstrate that photoirradiation and the use of an oxalate electron source are essential for  $\bullet\text{CF}_3$  generation. Interestingly, the production of  $\bullet\text{CF}_3$  was observed in a photoirradiated solution devoid of the photocatalyst (entry 4). This result may be due to the photocleavage of oxalate through the weak  $n-\pi^*$  transition.<sup>65</sup> However, the strong overlap between the MLCT transition band of [Ir(dfppy)<sub>2</sub>(bpy)]PF<sub>6</sub> and the photochemical action spectrum for trifluoromethylation provides convincing evidence that the cleavage of oxalate occurs mainly through photoredox catalysis (Figure 4). Similar results were obtained for [Ru(phen)<sub>3</sub>]Cl<sub>2</sub>. Of the tested photocatalysts, [Ir(dfppy)<sub>2</sub>(bpy)]PF<sub>6</sub> provided the best yield (entry 5). The comparison of this yield with the value obtained for *fac*-Ir(ppy)<sub>3</sub> (entry 7) suggests that reductive quenching of the photocatalyst may be superior to oxidative quenching for the coreactant-mediated  $\bullet\text{CF}_3$  generation, which is consistent with the kinetic analysis for electron transfer (i.e., Figure 3). Note also that the observation that [Ir(dfppy)<sub>2</sub>(bpy)]PF<sub>6</sub> provides the highest yield is in accordance with the conclusion that it exhibits the largest rate constant for reductive quenching by TBAOX. However, although it is tempting to rationalize the catalytic activities on the basis of the initial electron transfer processes, further investigations with optimized reaction conditions are required.

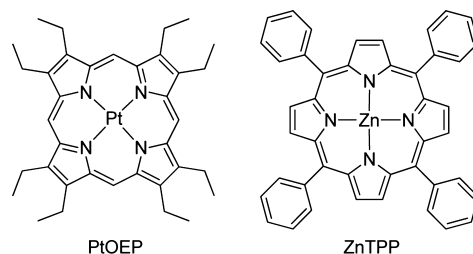
In the final phase of this study,  $\bullet\text{CF}_3$  generation was performed in the presence of 5,10,15,20-tetraphenyl-21H,23H-porphine zinc (ZnTPP) and 2,3,7,8,12,13,17,18-octaethyl-21H,23H-porphine platinum (PtOEP) as narrow-bandgap photocatalysts. These porphyrin complexes exhibited visible absorption in the orange-red regions due to the presence of their characteristic Q-bands ( $\lambda_{\text{abs}}$  ( $\epsilon$ ): ZnTPP, 556 nm (5100  $\text{M}^{-1} \text{ cm}^{-1}$ ); PtOEP, 533 nm (4900,  $\text{M}^{-1} \text{ cm}^{-1}$ ); see Figure S6). It was envisioned that these photocatalysts would oxidize oxalate because the  $E_{\text{red}}^*$  value was more positive than the  $E_{\text{ox}}$  value of oxalate.<sup>66</sup> Indeed, our photoluminescence quenching experiments revealed that the addition of TBAOX leads to decreases in the photoluminescence intensities of ZnTPP and PtOEP (Figure S6). The recovery of the ground-state catalysts from the one-electron-reduced species is possible through exergonic electron transfer to CF<sub>3</sub>I (Figure S2). Photoirradiation of the reaction mixtures containing ZnTPP and PtOEP employing green (1 W) or red (5 W) LEDs furnished trifluoromethylated products in yields in the range 53–75% (see entries 9–12 in Table 1). The use of green LEDs resulted in higher yields, which is most likely due to the better spectral overlaps with the Q-bands of ZnTPP and PtOEP. The scope of the reaction with PtOEP as a photocatalyst was also examined for a variety of substrates, including alkenes containing hydroxyl (**5**), epoxide (**6**), ester (**7** and **8**), amine (**9**), thiourea (**10**), and carbamate (**11**) groups (Table 2). Product analyses employing <sup>19</sup>F NMR spectroscopy indicated that the strategy is amenable to the presence of a broad range of functionalities, although yields remained low. Further optimization of the reaction

Table 1. Photoredox Catalytic Generation of Trifluoromethyl Radicals in the Presence of Oxalate Coreactant<sup>a</sup>

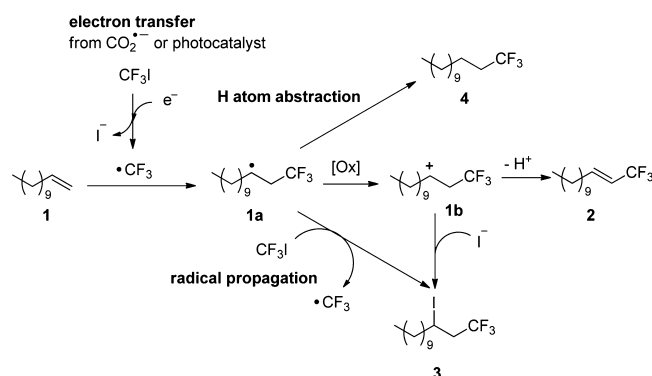


entry	photocatalyst	electron source	light source	yield (%) <sup>b</sup>		
				1	2	3
1	[Ru(phen) <sub>3</sub> ]Cl <sub>2</sub>	TBAOX	blue LEDs	13		73
2	[Ru(phen) <sub>3</sub> ]Cl <sub>2</sub>	TBAOX	no light	67		
3	[Ru(phen) <sub>3</sub> ]Cl <sub>2</sub>	no TBAOX	blue LEDs	60		
4	no photocatalyst	TBAOX	blue LEDs	29	37	9
5	[Ir(dfppy) <sub>2</sub> (bpy)]PF <sub>6</sub>	TBAOX	blue LEDs		37	56
6	[Ir(dfppy) <sub>2</sub> (bpy)]PF <sub>6</sub>	no TBAOX	blue LEDs	63		
7	<i>fac</i> -Ir(ppy) <sub>3</sub>	TBAOX	blue LEDs		19	48
8	<i>fac</i> -Ir(ppy) <sub>3</sub>	no TBAOX	blue LEDs	41		17
9	PtOEP	TBAOX	red LEDs	13	29	26
10	PtOEP	TBAOX	green LEDs		30	50
11	ZnTPP	TBAOX	red LEDs		24	37
12	ZnTPP	TBAOX	green LEDs		27	37

<sup>a</sup>Ar-saturated CH<sub>3</sub>CN solutions (2.0 mL) containing 0.50 mmol substrate, 1.5 mmol CF<sub>3</sub>I, 0.0050 mmol catalyst, and 1.3 mmol electron source were photoirradiated using LEDs for 24 h at room temperature. LED power: blue LEDs, 4 W; green LEDs, 1 W; red LEDs, 5 W. <sup>b</sup>GC yields determined using dodecane as an internal standard. We also observed the formation of hydrotrifluoromethylated product (4, 2–10%) along with several unidentified compounds.



### Scheme 2. Plausible Mechanism for the Syntheses of the Trifluoromethylated Product 2, Iodotrifluoromethylated Product 3, and Hydrotrifluoromethylated Product 4



conditions, including polarity of the solvent, may improve the catalytic performance. It should be underscored that this is the first demonstration of photoredox catalytic trifluoromethylation performed under low-energy photoirradiation.

### III. SUMMARY AND CONCLUSIONS

To summarize, we have developed a coreactant strategy for the photocatalytic generation of trifluoromethyl radicals. This coreactant strategy involves the reductive and oxidative quenching of photocatalysts by oxalate and CF<sub>3</sub>I, respectively.

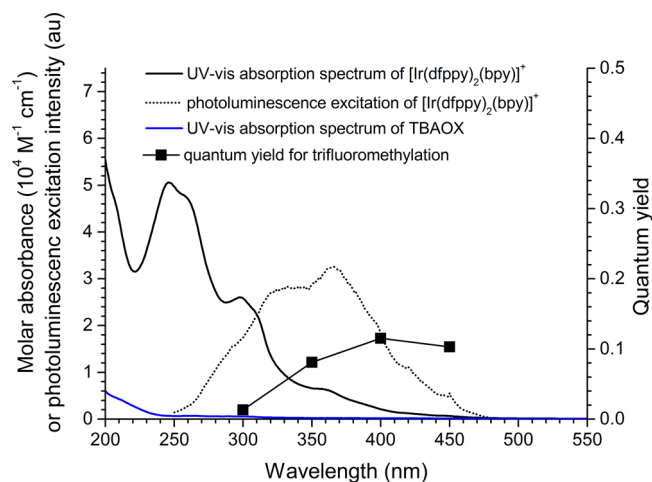


**Figure 4.** A comparison of the UV-vis absorption spectra of [Ir(dfppy)<sub>2</sub>(bpy)]PF<sub>6</sub> (black solid curve) and TBAOX (blue solid curve) with the photoluminescence excitation spectrum (dotted line) and the photochemical action spectrum (filled squares) of [Ir(dfppy)<sub>2</sub>(bpy)]<sup>+</sup>, which plots the quantum yields of the photocatalytic generation of •CF<sub>3</sub> in the presence of TBAOX.

In the case of the reductive quenching pathway, catalytic turnover is completed by the neutralization of the one-electron-reduced catalysts through exergonic electron transfer to CF<sub>3</sub>I. In the case of the oxidative quenching mechanism, electron

**Table 2. Substrate Scope of the Coreactant-Mediated Photoredox Catalytic Trifluoromethylation of a Variety of Alkenes<sup>a</sup>**

$$\text{CH}_2=\text{CH-R} \xrightarrow[\text{CH}_3\text{CN (0.25 M)}]{\begin{array}{l} 1.0 \text{ mol \% PtOEP} \\ 2.6 \text{ equiv TBAOX} \\ 3.0 \text{ equiv CF}_3\text{I} \end{array}} \text{F}_3\text{C-CH=CH-R} + \text{F}_3\text{C-CH}_2\text{-CH}_2\text{-R}$$
 green LEDs  
r.t., 24 h

entry	substrate	yield (%) <sup>b</sup>
5		92
6		81
7		70
8		67
9		41
10		47
11		21

<sup>a</sup>Ar-saturated CH<sub>3</sub>CN solutions (2.0 mL) containing 0.50 mmol substrate, 1.5 mmol CF<sub>3</sub>I, 0.0050 mmol PtOEP, and 1.3 mmol TBAOX were photoirradiated using green LEDs (1 W) for 24 h at room temperature. <sup>b</sup>Yields were determined by employing <sup>19</sup>F NMR spectroscopy with 1,4-difluorobenzene as an internal standard. Hydrotrifluoromethylation products might be produced, but they were not distinguishable in our <sup>19</sup>F NMR experiments.

donation by oxalate serves to restore the ground-state photocatalyst from the one-electron-oxidized species. In both pathways, the oxidation of oxalate promotes decarboxylative generation of the highly reducing CO<sub>2</sub><sup>•-</sup> species, which can then produce •CF<sub>3</sub> from CF<sub>3</sub>I (i.e., CO<sub>2</sub><sup>•-</sup> + CF<sub>3</sub>I → CO<sub>2</sub> + •CF<sub>3</sub> + I<sup>-</sup>). Overall, the net reaction is two-electron transfer from oxalate to two equivalents of CF<sub>3</sub>I (i.e., C<sub>2</sub>O<sub>4</sub><sup>2-</sup> + 2 CF<sub>3</sub>I → 2 CO<sub>2</sub> + 2 •CF<sub>3</sub> + 2 I<sup>-</sup>) irrespective of the quenching mechanism. The process is steered by the photoirradiation of photocatalysts with moderately positive excited-state reduction potentials ( $E_{\text{red}}^* > 0.21 \text{ V vs SCE}$ ). We established the thermodynamic and kinetic parameters of the electron transfer processes in the generation of •CF<sub>3</sub> species through electrochemical and transient photoluminescence studies. Our investigation of the mechanism revealed dominance of the reductive quenching pathway over the oxidative quenching pathway, an observation consistent with the thermodynamic prediction made from the Rehm–Weller terminology. Of importance is decoupling of a reductant and a photon-absorption species, which enables wide versatility in the selection of available photocatalysts. By taking advantage of the alleviated thermodynamic conditions, we successfully demonstrated the production of the thermodynamically challenging •CF<sub>3</sub> upon low-energy photoirradiation. Although the synthetic possibilities of this strategy have not yet been fully explored, we conclude that the coreactant strategy would be of great value for a broad range of radical transformations involving  $\pi$ -conjugated substrates.

## IV. EXPERIMENTAL SECTION

**Materials and Synthesis.** Commercially available chemicals, including *fac*-Ir(ppy)<sub>3</sub>, [Ru(phen)<sub>3</sub>]Cl<sub>2</sub>, ZnTPP, and PtOEP, were used without further purification. The syntheses of [Ir(dfppy)<sub>2</sub>(bpy)]PF<sub>6</sub><sup>67</sup> and TBAOX<sup>17,55,56</sup> were performed following the methods reported previously. All glassware and magnetic stir bars were thoroughly dried in a convection oven. Anhydrous acetonitrile was purchased and used as received. Reactions were monitored using thin layer chromatography (TLC). Commercial TLC plates were developed, and the spots were visualized under UV illumination at 254 or 365 nm and stained with phosphomolybdic acid and *p*-anisaldehyde reagents. <sup>1</sup>H NMR spectra were referenced to deuterated solvents.

**General Procedure for the Photoreactions.** An oven-dried resealable tube equipped with a magnetic stir bar was charged with 0.50 mmol 1-dodecene, 1.3 mmol TBAOX, 1.0 mol % photocatalyst, and 2.0 mL of anhydrous acetonitrile. After deaeration by bubbling with Ar, 1.5 mmol CF<sub>3</sub>I was injected into the reaction mixture using a gastight syringe. The reaction mixture was placed under LED irradiation at room temperature for 24 h (blue LEDs, ~450 nm and 4 W; green LEDs, ~550 nm and 1 W; red LEDs, ~650 nm and 5 W). Product analysis was performed with GC–MS spectrometry and <sup>19</sup>F NMR spectroscopy using dodecane and 1,4-difluorobenzene as internal standards, respectively.

**Spectroscopic Identification Data.** 2: colorless oil; <sup>1</sup>H NMR (400 MHz, CDCl<sub>3</sub>)  $\delta$  6.38 (dtq,  $J = 15.9, 6.8, 2.0 \text{ Hz}$ , 1H), 5.60 (dqt,  $J = 15.9, 6.4 (J_{\text{H-F}}), 1.6 \text{ Hz}$ , 1H), 2.19–2.10 (m, 2H), 1.47–1.39 (m, 2H), 1.33–1.24 (m, 14H), 0.88 (t,  $J = 6.4 \text{ Hz}$ , 3H); <sup>13</sup>C NMR (101 MHz, CDCl<sub>3</sub>)  $\delta$  141.0 (q,  $J = 6.4 \text{ Hz}$ ), 123.4 (q,  $J = 270.0 \text{ Hz}$ ), 118.6 (q,  $J = 33.2 \text{ Hz}$ ), 32.2, 31.7, 29.9, 29.8, 29.7, 29.61, 29.3, 28.3, 23.0, 14.3; <sup>19</sup>F NMR (377 MHz, CDCl<sub>3</sub>)  $\delta$  -64.3; FTIR (neat)  $\nu_{\text{max}} = 2928, 2857, 1273, 1122 \text{ cm}^{-1}$ ; HRMS  $m/z$  (EI) calcd for C<sub>13</sub>H<sub>23</sub>F<sub>3</sub> [M<sup>+</sup>] 236.1752, found 236.1750;  $R_f = 0.95$  (hexanes).

3: colorless oil; <sup>1</sup>H NMR (400 MHz, CDCl<sub>3</sub>)  $\delta$  4.24–4.16 (m, 1H), 2.98–2.70 (m, 2H), 1.85–1.68 (m, 2H), 1.59–1.22 (m, 16H), 0.89 (t,  $J = 7.2 \text{ Hz}$ , 3H); <sup>13</sup>C NMR (101 MHz, CDCl<sub>3</sub>)  $\delta$  125.8 (q,  $J = 279.8 \text{ Hz}$ ), 45.2 (q,  $J = 28.2 \text{ Hz}$ ), 39.9, 32.1, 29.8, 29.8, 29.7, 29.6, 29.6, 28.8, 22.9, 22.0 (q,  $J = 2.7 \text{ Hz}$ ), 14.3; FTIR (neat)  $\nu_{\text{max}} = 2926, 2856, 1256, 1149 \text{ cm}^{-1}$ ; HRMS  $m/z$  (EI) calcd for C<sub>13</sub>H<sub>24</sub>F<sub>3</sub>I [M<sup>+</sup>] 364.0875, found 364.0877;  $R_f = 0.90$  (hexanes).

**Spectroscopic Measurements.** The photocatalyst solutions were prepared by dissolution in CH<sub>3</sub>CN to concentrations of 10 mM, 1 mM, 100  $\mu$ M, and 10  $\mu$ M. The 10  $\mu$ M solutions were used for spectroscopic measurements unless otherwise noted. A 1 cm  $\times$  1 cm fluorimeter cell with a 14/20 joint that could accommodate a rubber septum was used in the steady-state optical measurements. UV–vis absorption spectra were collected at 298 K. Photoluminescence spectra were obtained at room temperature. The photocatalyst solutions were excited at the following wavelengths: [Ir(dfppy)<sub>2</sub>(bpy)]PF<sub>6</sub>, 365 nm; [Ru(phen)<sub>3</sub>]Cl<sub>2</sub>, 468 nm; *fac*-Ir(ppy)<sub>3</sub>, 380 nm. The solutions were thoroughly degassed by bubbling with Ar prior to performing the measurements. Ar-saturated 50  $\mu$ M solutions (CH<sub>3</sub>CN) were used to determine the photoluminescence lifetimes. Photoluminescence decay traces were acquired with time-correlated single-photon-counting (TCSPC) techniques. A 377 nm diode laser was used as the excitation source. The photoluminescence signals were obtained with an automated motorized monochromator. Photoluminescence decay profiles were analyzed using mono- or biexponential decay models.

### Determination of Photochemical Quantum Yields (PCQYs).

The quantum yields for trifluoromethylation were determined by performing standard ferrioxalate actinometry. A 0.0060 M K<sub>3</sub>[Fe(C<sub>2</sub>O<sub>4</sub>)<sub>3</sub>] solution was used as the chemical actinometer; 500  $\mu$ L of this K<sub>3</sub>[Fe(C<sub>2</sub>O<sub>4</sub>)<sub>3</sub>] solution was transferred to a 1 cm  $\times$  1 mm quartz cell, and the solution was photoirradiated with a monochromatized beam at 300, 350, 400, and 450 nm for 30 s. Then, the same amount of 1% 1,10-phenanthroline in sodium acetate buffer solution (4.09 g of CH<sub>3</sub>COONa dissolved in 18 mL of 0.50 M H<sub>2</sub>SO<sub>4</sub> and 32 mL of distilled water) was added and stored in the dark for 1 h. The absorbance changes at 510 nm were recorded; inserting these values



into eq 4 returned light intensities of  $1.1 \times 10^{-8}$  einstein  $s^{-1}$  at 300 nm,  $1.0 \times 10^{-8}$  einstein  $s^{-1}$  at 350 nm,  $9.7 \times 10^{-9}$  einstein  $s^{-1}$  at 400 nm, and  $9.8 \times 10^{-9}$  einstein  $s^{-1}$  at 450 nm:

$$\text{light intensity } (I_0, \text{ einstein } s^{-1}) \\ = (\Delta\text{Abs}(510\text{nm}) \times V) / (\Phi \times 11050 \text{ M}^{-1}\text{cm}^{-1} \times \Delta t) \quad (4)$$

In eq 4,  $\Delta\text{Abs}(510 \text{ nm})$ ,  $V$ ,  $\Phi$ , and  $\Delta t$  are the absorbance change at 510 nm, volume (L), quantum yield (1.1) of the ferrioxalate actinometer at 420 nm, and photoirradiation time (s), respectively. Ar-saturated acetonitrile solutions (2.0 mL) containing 0.50 mmol 1-dodecene, 1.3 mmol TBAOX, 1.5 mmol  $\text{CF}_3\text{I}$ , and 1.0 mol % photocatalyst were photoirradiated under identical conditions for 1 h. The concentrations of the products resulting from the trapping of trifluoromethyl radicals were quantified with GC-MS by using dodecane as an internal standard, and then inserted into eq 5

$$\text{PCQY} = \frac{[\text{product}] \times V}{I \times \Delta t} \quad (5)$$

In eq 5, [product] is the molar concentration of the products,  $\Delta t$  (s) is the photoirradiated time,  $V$  is the volume of the solution (L), and  $I_0$  is the light intensity obtained with eq 4 (einstein  $s^{-1}$ ).

**Electrochemical Characterization.** Cyclic voltammetry and differential pulse voltammetry experiments were carried out by using a three-electrode cell assembly. A Pt wire and a Pt microdisc were used as the counter and working electrodes, respectively. A Ag/AgNO<sub>3</sub> couple was used as the pseudo reference electrode. Measurements were carried out in Ar-saturated CH<sub>3</sub>CN (2.0 mL) by using 0.10 M tetra-*n*-butylammonium hexafluorophosphate (Bu<sub>4</sub>NPF<sub>6</sub>) as the supporting electrolyte at scan rates of 100 mV/s (cyclic voltammetry) and 4.0 mV/s (differential pulse voltammetry). The concentration was 2.0 mM, and a ferrocenium/ferrocene couple was employed as the external reference.

## ■ ASSOCIATED CONTENT

### ■ Supporting Information

The Supporting Information is available free of charge on the ACS Publications website at DOI: 10.1021/acs.joc.6b00966.

UV-vis absorption spectra, cyclic and differential pulse voltammograms, steady-state photoluminescence spectra, photoluminescence quenching experiment results, a comparison of the UV-vis absorption spectrum of [Ru(phen)<sub>3</sub>]<sup>2+</sup> and the photochemical action spectrum for trifluoromethylation, spectroscopic data for ZnTPP and PtOEP, and copies of <sup>1</sup>H and <sup>13</sup>C NMR spectra (PDF)

## ■ AUTHOR INFORMATION

### Corresponding Authors

\*E-mail: ejcho@cau.ac.kr.

\*E-mail: odds2@ewha.ac.kr.

### Notes

The authors declare no competing financial interest.

## ■ ACKNOWLEDGMENTS

Y.Y. acknowledges a grant from the Ewha Womans University (1-2015-0447-001-1).

## ■ REFERENCES

- (1) Fukuzumi, S.; Ohkubo, K. *Chem. Sci.* **2013**, *4*, 561–574.
- (2) Fukuzumi, S.; Ohkubo, K. *Org. Biomol. Chem.* **2014**, *12*, 6059–6071.
- (3) Hoffmann, N. *Photochem. Photobiol. Sci.* **2012**, *11*, 1613–1641.
- (4) Hopkinson, M. N.; Sahoo, B.; Li, J.-L.; Glorius, F. *Chem. - Eur. J.* **2014**, *20*, 3874–3886.

- (5) Inagaki, A.; Akita, M. *Coord. Chem. Rev.* **2010**, *254*, 1220–1239.
- (6) Ischay, M. A.; Yoon, T. P. *Eur. J. Org. Chem.* **2012**, *2012*, 3359–3372.
- (7) Koike, T.; Akita, M. *Synlett* **2013**, *24*, 2492–2505.
- (8) Narayanam, J. M. R.; Stephenson, C. R. J. *Chem. Soc. Rev.* **2011**, *40*, 102–113.
- (9) Nicewicz, D. A.; Nguyen, T. M. *ACS Catal.* **2014**, *4*, 355–360.
- (10) Prier, C. K.; Rankic, D. A.; MacMillan, D. W. C. *Chem. Rev.* **2013**, *113*, 5322–5363.
- (11) Ravelli, D.; Dondi, D.; Fagnoni, M.; Albini, A. *Chem. Soc. Rev.* **2009**, *38*, 1999–2011.
- (12) Ravelli, D.; Fagnoni, M. *ChemCatChem* **2012**, *4*, 169–171.
- (13) Ravelli, D.; Fagnoni, M.; Albini, A. *Chem. Soc. Rev.* **2013**, *42*, 97–113.
- (14) Tucker, J. W.; Stephenson, C. R. J. *J. Org. Chem.* **2012**, *77*, 1617–1622.
- (15) Xi, Y.; Yi, H.; Lei, A. *Org. Biomol. Chem.* **2013**, *11*, 2387–2403.
- (16) Xie, J.; Jin, H.; Xu, P.; Zhu, C. *Tetrahedron Lett.* **2014**, *55*, 36–48.
- (17) Xuan, J.; Xiao, W.-J. *Angew. Chem., Int. Ed.* **2012**, *51*, 6828–6838.
- (18) Yoon, T. P. *ACS Catal.* **2013**, *3*, 895–902.
- (19) Yoon, T. P.; Ischay, M. A.; Du, J. *Nat. Chem.* **2010**, *2*, 527–532.
- (20) Zeitler, K. *Angew. Chem., Int. Ed.* **2009**, *48*, 9785–9789.
- (21) Xu, P.; Xie, J.; Xue, Q.; Pan, C.; Cheng, Y.; Zhu, C. *Chem. - Eur. J.* **2013**, *19*, 14039–14042.
- (22) Iqbal, N.; Jung, J.; Park, S.; Cho, E. J. *Angew. Chem., Int. Ed.* **2014**, *53*, 539–542.
- (23) Nagib, D. A.; Scott, M. E.; MacMillan, D. W. C. *J. Am. Chem. Soc.* **2009**, *131*, 10875–10877.
- (24) Yasu, Y.; Koike, T.; Akita, M. *Angew. Chem., Int. Ed.* **2012**, *51*, 9567–9571.
- (25) Jiang, H.; Cheng, Y.; Zhang, Y.; Yu, S. *Eur. J. Org. Chem.* **2013**, *2013*, 5485–5492.
- (26) Kanoufi, F.; Bard, A. J. *J. Phys. Chem. B* **1999**, *103*, 10469–10480.
- (27) Nagib, D. A.; MacMillan, D. W. C. *Nature* **2011**, *480*, 224–228.
- (28) Ye, Y.; Sanford, M. S. *J. Am. Chem. Soc.* **2012**, *134*, 9034–9037.
- (29) Carboni, A.; Dagousset, G.; Magnier, E.; Masson, G. *Org. Lett.* **2014**, *16*, 1240–1243.
- (30) Yasu, Y.; Arai, Y.; Tomita, R.; Koike, T.; Akita, M. *Org. Lett.* **2014**, *16*, 780–783.
- (31) Yasu, Y.; Koike, T.; Akita, M. *Chem. Commun.* **2013**, *49*, 2037–2039.
- (32) Pham, P. V.; Nagib, D. A.; MacMillan, D. W. C. *Angew. Chem., Int. Ed.* **2011**, *50*, 6119–6122.
- (33) Iqbal, N.; Choi, S.; Ko, E.; Cho, E. J. *Tetrahedron Lett.* **2012**, *53*, 2005–2008.
- (34) Iqbal, N.; Choi, S.; Kim, E.; Cho, E. J. *J. Org. Chem.* **2012**, *77*, 11383–11387.
- (35) Mizuta, S.; Verhoog, S.; Engle, K. M.; Khotavivattana, T.; O'Duill, M.; Wheelhouse, K.; Rassias, G.; Médebielle, M.; Gouverneur, V. *J. Am. Chem. Soc.* **2013**, *135*, 2505–2508.
- (36) Mizuta, S.; Engle, K. M.; Verhoog, S.; Galicia-López, O.; O'Duill, M.; Médebielle, M.; Wheelhouse, K.; Rassias, G.; Thompson, A. L.; Gouverneur, V. *Org. Lett.* **2013**, *15*, 1250–1253.
- (37) Mizuta, S.; Verhoog, S.; Wang, X.; Shibata, N.; Gouverneur, V.; Médebielle, M. *J. Fluorine Chem.* **2013**, *155*, 124–131.
- (38) Kim, E.; Choi, S.; Kim, H.; Cho, E. J. *Chem. - Eur. J.* **2013**, *19*, 6209–6212.
- (39) Choi, W. J.; Choi, S.; Ohkubo, K.; Fukuzumi, S.; Cho, E. J.; You, Y. *Chem. Sci.* **2015**, *6*, 1454–1464.
- (40) Haering, M.; Perez-Ruiz, R.; Jacobi von Wangelin, A.; Diaz, D. D. *Chem. Commun.* **2015**, *51*, 16848–16851.
- (41) Majek, M.; Faltermeier, U.; Dick, B.; Perez-Ruiz, R.; von Wangelin, A. J. *Chem. - Eur. J.* **2015**, *21*, 15496–15501.
- (42) Ghosh, I.; Ghosh, T.; Bardagi, J. I.; Koenig, B. *Science* **2014**, *346*, 725–728.

- (43) Goez, M.; Kerzig, C.; Naumann, R. *Angew. Chem., Int. Ed.* **2014**, *53*, 9914–9916.
- (44) Kerzig, C.; Goez, M. *Chem. Sci.* **2016**, *7*, 3862–3868.
- (45) Mulazzani, Q. G.; D'Angelantonio, M.; Venturi, M.; Hoffman, M. Z.; Rodgers, M. A. J. *J. Phys. Chem.* **1986**, *90*, 5347–5352.
- (46) Rubinstein, I.; Bard, A. J. *J. Am. Chem. Soc.* **1981**, *103*, 512–516.
- (47) Chang, M.-M.; Saji, T.; Bard, A. J. *J. Am. Chem. Soc.* **1977**, *99*, 5399–5403.
- (48) Krasna, A. I. *Photochem. Photobiol.* **1980**, *31*, 75–82.
- (49) Pina, F.; Mulazzani, Q. G.; Venturi, M.; Ciano, M.; Balzani, V. *Inorg. Chem.* **1985**, *24*, 848–851.
- (50) Andrieux, C. P.; Gelis, L.; Medebielle, M.; Pinson, J.; Saveant, J. M. *J. Am. Chem. Soc.* **1990**, *112*, 3509–3520.
- (51) Herrmann, J. M.; Mozzanega, M. N.; Pichat, P. *J. Photochem.* **1983**, *22*, 333–343.
- (52) Aguilar, C.; Urzua, U.; Koenig, C.; Vicuna, R. *Arch. Biochem. Biophys.* **1999**, *366*, 275–282.
- (53) Opaleye, O.; Rose, R.-S.; Whittaker, M. M.; Woo, E.-J.; Whittaker, J. W.; Pickersgill, R. W. *J. Biol. Chem.* **2006**, *281*, 6428–6433.
- (54) Woo, E.-J.; Dunwell, J. M.; Goodenough, P. W.; Marvier, A. C.; Pickersgill, R. W. *Nat. Struct. Biol.* **2000**, *7*, 1036–1040.
- (55) Moon, H. C.; Lodge, T. P.; Frisbie, C. D. *Chem. Mater.* **2014**, *26*, 5358–5364.
- (56) Qi, H.; Chang, J.; Abdelwahed, S. H.; Thakur, K.; Rathore, R.; Bard, A. J. *J. Am. Chem. Soc.* **2012**, *134*, 16265–16274.
- (57) Yamazaki-Nishida, S.; Kimura, M. *Bull. Chem. Soc. Jpn.* **1991**, *64*, 1840–1845.
- (58) Kimura, M.; Nishida, S. *J. Chem. Soc., Dalton Trans.* **1985**, 355–359.
- (59) Yamada, Y.; Miyahigashi, T.; Ohkubo, K.; Fukuzumi, S. *Phys. Chem. Chem. Phys.* **2012**, *14*, 10564–10571.
- (60) Yamada, Y.; Nomura, A.; Miyahigashi, T.; Fukuzumi, S. *Chem. Commun.* **2012**, *48*, 8329–8331.
- (61) Wilger, D. J.; Gesmundo, N. J.; Nicewicz, D. A. *Chem. Sci.* **2013**, *4*, 3160–3165.
- (62) Marcus, R. A.; Eyring, H. *Annu. Rev. Phys. Chem.* **1964**, *15*, 155–196.
- (63) Marcus, R. A.; Sutin, N. *Biochim. Biophys. Acta, Rev. Bioenerg.* **1985**, *811*, 265–322.
- (64) Murakami, M.; Ohkubo, K.; Fukuzumi, S. *Chem. - Eur. J.* **2010**, *16*, 7820–7832.
- (65) Chang, M. C. Y.; Miller, S. E.; Carpenter, S. D.; Stubbe, J.; Nocera, D. G. *J. Org. Chem.* **2002**, *67*, 6820–6822.
- (66) The excited-state reduction potential of ZnTPP was determined to be 0.86 V vs SCE (Figures S2 and S3). In the case of PtOEP, the reduction potential could not be determined due to the lack of the reduction process within the electrochemical window of the acetonitrile solvent.
- (67) You, Y.; Lee, S.; Kim, T.; Ohkubo, K.; Chae, W.-S.; Fukuzumi, S.; Jhon, G.-J.; Nam, W.; Lippard, S. J. *J. Am. Chem. Soc.* **2011**, *133*, 18328–18342.